

Ignition of ultra-lean premixed hydrogen/air by an impinging hot jet

Sayan Biswas, Li Qiao*

School of Aeronautics and Astronautics, Purdue University, West Lafayette, IN, USA



HIGHLIGHTS

- Ignition characteristics by impinging hot turbulent jet in a dual chamber system are proposed.
- The ratio of impinging distance to the nozzle diameter, H/D and the impinging angle, θ are examined.
- Using impinging jet ignition, a lower flammability limit of hydrogen/air is achieved.
- Numerical simulation of jet impingement process is performed.

ARTICLE INFO

Keywords:

Turbulent jet ignition (TJI)
Impinging jet ignition
Ultra-lean combustion
Pre-chamber combustion
Reacting impinging jet

ABSTRACT

The ignition characteristics of a hot turbulent jet impinging on a flat plate surrounded by an ultra-lean premixed H_2 /air was studied both experimentally and numerically. The hot turbulent jet was generated by burning a small quantity of stoichiometric H_2 /air mixture in a separate small volume called the pre-chamber. The higher pressure resulting from pre-chamber combustion pushed the combustion products into the main chamber through a small nozzle (0.75–4.5 mm in diameter) in the form of a hot turbulent jet, which then impinged on a flat plate. Six different plates with varying impinging heights and angles were used. Two important parameters controlling the impinging characteristics of the jet, the ratio of the impinging distance to the nozzle diameter, H/D and the impinging angle, θ were examined. Simultaneous high-speed Schlieren and OH^* chemiluminescence imaging were applied to visualize the jet penetration/impinging and ignition process inside the main combustion chamber. Results illustrate the existence of two distinct types of ignition mechanisms. If the impinging distance is short and the hot turbulent jet hits the plate with high enough momentum, the temperature increases around the stagnation point and ignition starts from this impinging region. However, if the impinging distance is long, the hot turbulent jet mixes with the ambient unburned H_2 /air in the main chamber and ignites the mixture at the upstream from the plate. For such type of ignition, the impinging plate has a minimum role on main chamber ignition. Employing the stagnation point ignition, a leaner limit of H_2 /air in the main chamber was achieved. Numerical modeling of the turbulent hot jet impingement process was carried out to explain the impinging jet ignition mechanism. It was found that H/D ratio was the controlling parameter between the two ignition mechanisms. The limiting H/D ratio was found to be 21.6, below which ignition occurred via jet impingement. Unlike the H/D ratio, the impinging angle did not affect the ignition mechanism; however, it affected the main chamber burn time.

1. Introduction

Pre-chamber turbulent jet ignition (TJI) has been used as an advanced ignition technique for various combustion systems with applications ranging from pulse detonation engines [1], wave rotor combustor explosions [2], to supersonic combustors [3] and lean-burn natural gas engines [4]. The main reason that TJI has become attractive to gas engine manufacturers is that hot jet ignition can achieve faster burn rates due to the ignition system producing distributed ignition sites, which consume the main charge more rapidly and with minimal

combustion variability. Compared to a conventional spark plug, the hot jet has a much larger surface area leading to multiple ignition sites on its surface which can enhance the probability of successful ignition and cause faster flame propagation and heat release. Over the last few decades, pre-chamber TJI had technologically advanced from conceptual design phase to actual gas engines. The early designs developed by Gussak [5], Oppenheim [6] and Wolfhard [7] showed the promise of lean ignition by a hot turbulent jet. Later, Ghoneim [8], Pitt [9], Yamaguchi [10], Sadanandan [11], Toulson [12], Gholamisheeri [13], Attard [14], Gentz [15], Perera [16], Carpio [17], Shah [18], Karimi

* Corresponding author.

E-mail address: lqiao@purdue.edu (L. Qiao).

[2], Vedula [19], and Biswas [20] further investigated in detail the parametric effects of turbulent jet ignition in laboratory-scale prototype combustors and at engine relevant conditions. These studies support that TJI possesses several advantages over traditional spark ignition such as higher ignition probability, multiple ignition kernels, and faster burn rates.

TJI, however, is a complicated phenomenon and our knowledge is far from complete. Several studies have examined the fundamental mechanisms behind TJI – the complex coupling between turbulent mixing and chemical reactions [13,20,21]. For example, the jet containing hot combustion products penetrates the lean fuel/air mixture that resides in the main chamber, providing a high-temperature environment for mixing and ignition. Depending on the operating condition, the jet may or may not contain active radicals such as H, O, and OH, which initiate chain-branching reactions [5,22]. We can expect that several factors, such as the radicals which are important for ignition chemistry, as well as the mixing process between the hot burned products and the cold fresh lean mixtures, all affect the ignition process.

TJI becomes even more complicated in an engine environment [23,24]. Along with turbulent mixing and complex chemical processes, the wall effect can be significant. Inside the small volume of the combustion chamber in the engine, the effect of confinement and chances of jet impingement becomes predominant. The hot jet issued from the pre-chamber may impinge onto the surface of the piston head or the wall of the main engine during the cycle. This is particularly true when multiple jets (typically 6–12) generated from pre-chamber combustion are utilized [25,26]. Motivated by this, the present study intended to understand the impact of impingement on TJI ignition process which has great significance for automotive and gas engine applications. In particular, the study focused on two variables: (1) the location of the impinging surface from the nozzle exit, which represents the motion of the piston head i.e. location of piston head at different crank angles, and (2) the angle of the impinging surface, which implies various design profiles of the piston head.

Although a large number of literature have discussed the physics of an impinging liquid or gas jet onto a plate from fundamental fluid dynamics and heat transfer standpoint, few studies have examined ignition of premixed fuel/air mixtures by an impinging hot jet. Most of the existing literature focused on heating of materials by steady flame impingement, a practice used in processing industries [27,28]. Among the very few studies that are relevant to reacting turbulent hot jet, Tajik and Hindsageri [29] numerically investigated the heat transfer and emissions characteristics of impinging radial jet reattachment combustion (RJRC) flame. RJRC flame jet is used in applications where the impingement surface is delicate and demands low impingement pressure. They found that the peak heat flux and the concentrations of NO_x and CO emissions increased significantly with the increase in the Reynolds number. Additionally, as the nozzle-tip-to-plate spacing increased, the peak heat flux and the pressure coefficient decreased. Wang [30] studied the ignition process using a methane diffusion impinging flame and found the impinging distance played a key role in determining the ignition timing. Despite these studies, no work has been done on the ignition characteristics of a lean mixture by a highly-turbulent impinging hot jet. This motivated us to investigate the ignition of premixed H₂/air using a hot turbulent jet impinging on a flat plate. The knowledge developed from this work will be helpful for future pre-chamber designs and optimization for automotive and gas engine applications.

The goal of the present study was to examine the ignition behavior of ultra-lean H₂/air mixtures by a turbulent hot jet impinging onto a surface. Six different plates with varying heights and angles were used. In the experiment, the higher pressure resulting from pre-chamber combustion of stoichiometric H₂/air pushed the combustion products into the main chamber through a small nozzle (0.75–4.5 mm in diameter) in the form of a hot turbulent jet, which then impinged onto a flat plate which was placed inside the main combustion chamber filled

with lean H₂/air mixture. Depending on the impinging distance and impinging angle, two ignition mechanisms exist: one is via impingement for which ignition takes place near the impinging point, and the other is via typical turbulent jet ignition where ignition takes place on the lateral sides of the hot jet before it hits the impinging plate. The effect of the different ignition mechanisms on the lean limit of the main chamber H₂/air mixture was investigated. Furthermore, detailed numerical simulations were carried out to understand the impinging jet dynamics which helped to explain the experimental observations.

2. Experimental methods

The schematic of the experimental setup and the dual combustion chamber are shown in Fig. 1(a) and (b) respectively. The experimental setup was thoroughly described in our earlier studies [31–36]. Thus, only a brief description is presented here. A small volume stainless steel pre-chamber was mounted on top of a carbon steel main chamber. The main chamber to pre-chamber volume ratio was 100:1. A stainless steel nozzle plate was placed between the two chambers to separate them. In our current experiment, a variety of nozzle diameters, D ranging from 0.75 to 4.5 mm (0.75, 1, 1.5, 2, 2.25, 3, 4.5 mm) were used. However, the ignition characteristics had been primarily investigated in detail for a nozzle diameter of 3 mm and 1.5 mm. Later, the effect of H/D ratio on ignition behavior was explored using other nozzle diameters. Thus, most of the experimental and numerical visualizations were for 3 mm diameter nozzle, unless otherwise stated. Initially, H₂/air mixtures in both chambers were kept at room temperature. The stoichiometric H₂/air mixture in the pre-chamber was ignited by an electric spark (using a Bosch Iridium spark plug) generated near the top of the pre-chamber. Once the spark ignited the pre-chamber fuel/air mixture, the combustion products entered the main chamber in the form of a hot jet, which, then impinged on the flat plate placed inside the main chamber and ignited the ultra-lean H₂/air in the main chamber. The lean limit for each nozzle/plate combination was found by gradually reducing the H₂/air equivalence ratio inside the main chamber until ignition could not occur anymore. Note the H₂/air equivalence ratio of the pre-chamber mixture was fixed at $\phi = 1$ for all cases, whereas the H₂/air equivalence ratio of the main chamber mixture was varied from $\phi = 0.5$ to the lean limit for the corresponding test condition. The equivalence ratio in both the pre-chamber and main chamber was determined using the partial pressure method. A high-accuracy, low-cost pressure transducer (Kulite XTEL 190, Omega PX51) was used to control the fuel/air ratio. The stoichiometric pre-chamber mixture was prepared in a separate mixing chamber.

Six different stainless-steel impinging plates were used in the present study. The schematic of the impinging plates and plate numberings are shown in Fig. 1(c). In the plate nomenclature, there are two quantities. The first quantity after ‘H’ denotes impinging height/distance in inch, which is the vertical distance between the nozzle exit and the impinging plate along the nozzle centerline. The second quantity, ‘ α ’ denotes the impinging angle, which is the angle of the impinging plane with the horizontal direction as illustrated in Fig. 1(b). Using this plate nomenclature scheme, H2.2 α 0° denotes an impinging plate 2.2 in. away from the jet exit, and the impinging plane makes an angle zero degree with the horizontal direction.

The dimensions of the six impinging plates are reported in Table 1. For all the plates, the base length, width, and thickness were identical, which were 3, 2, and 0.2 in., respectively. The impinging surface was smooth and free from any irregularities. After every 5 tests, the surface was thoroughly cleaned to avoid water deposition which is the only product of lean hydrogen combustion. The two most important geometric parameters of the impinging jet experiment were H/D ratio and impinging angle, θ . The ignition results with and without an impinging plate were compared. The cases without an impinging plate were denoted as ‘NP.’

The main chamber was installed with four rectangular

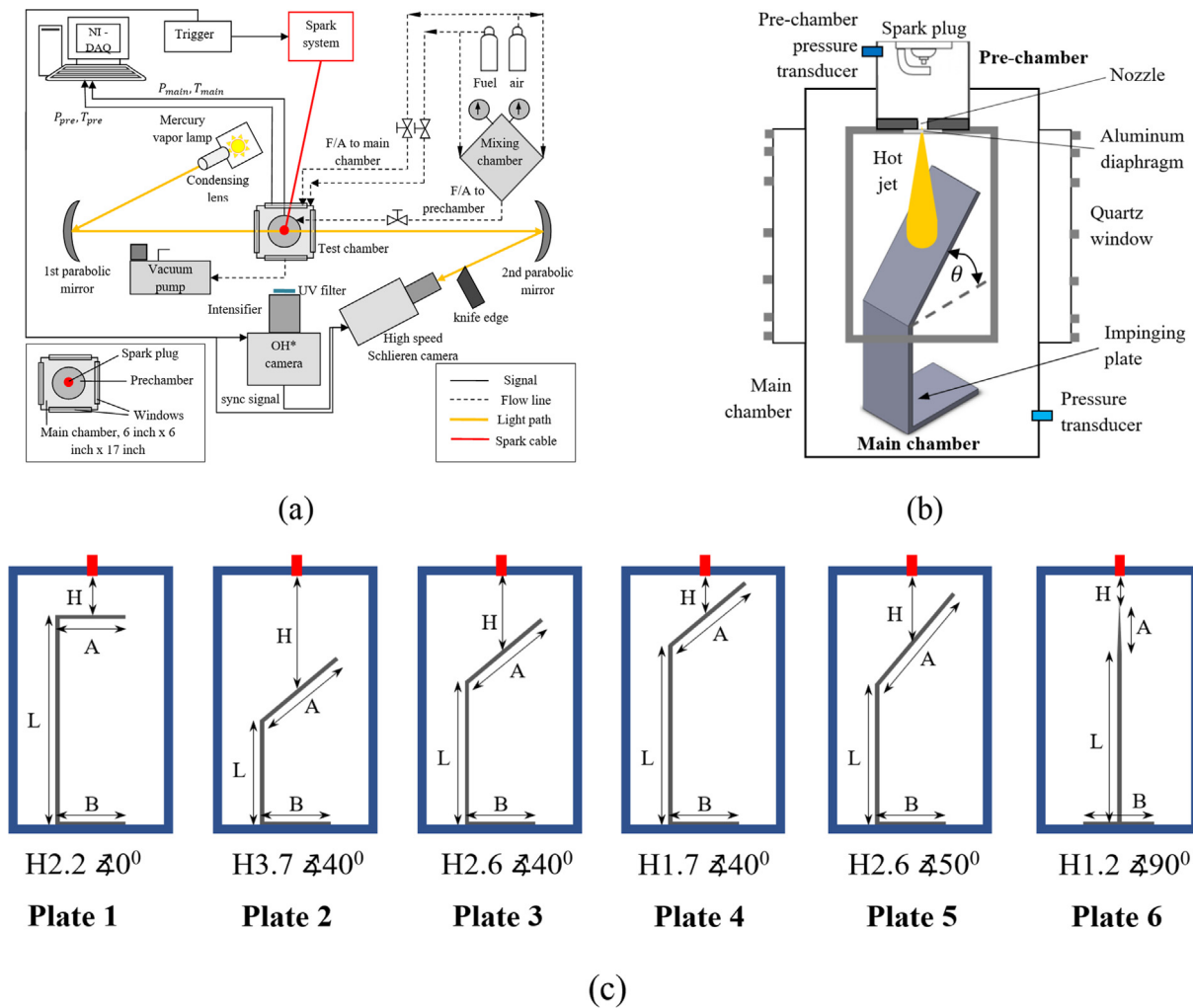


Fig. 1. Schematic of the (a) experimental setup, (b) the dual combustion chamber with an impinging plate inside the main chamber, (c) six different impinging plates.

Table 1
Nomenclature and dimensions of six different impinging plates.

Plate #	Plate name	Impinging surface length, A, in.	Straight section, L, in.	Distance from nozzle exit, D, in.	θ
1	H2.2 $\nabla 0^\circ$	3	14.8	2.2	0°
2	H3.7 $\nabla 40^\circ$	3.9	15	3.7	40°
3	H2.6 $\nabla 40^\circ$	3.9	16	2.6	40°
4	H1.7 $\nabla 40^\circ$	3.9	17	1.7	40°
5	H2.6 $\nabla 50^\circ$	4.7	14.9	2.6	50°
6	H1.2 $\nabla 90^\circ$	0	15.8	1.2	90°

(5.5 × 3.5 × 0.75) quartz windows (type GE124) on its sides for optical access. One pair of the windows were used for the z-type Schlieren system, and the other was for OH* chemiluminescence measurement. A customized trigger box synchronized with the pre-chamber CDI spark ignition system sent a master trigger to two high-speed cameras for simultaneous Schlieren and OH* chemiluminescence imaging. The high-speed Schlieren technique was utilized to visualize the evolution of the hot jet as well as the ignition process in the main chamber. The

system consisted of a 100 W (ARC HAS-150 HP) mercury lamp light source with a condensing lens, two concave parabolic mirrors (15.24 cm diameter, focal length 1.2 m), and a high-speed digital camera (Vision Research Phantom v7). The Schlieren images were captured with a resolution of 800 × 720 pixels with a frame rate up to 12,000 fps. The high-speed OH* chemiluminescence measurement provided a better view of the ignition and flame propagation processes. Moreover, the OH* images were used to mark the onset of ignition in the main chamber. A high-speed camera (Vision Research Phantom v640), along with video-scope gated image intensifier (VS4-1845HS) with 105 mm UV lens, were utilized to detect OH* signals at a very narrow band 386 ± 10 nm detection limit. The intensifier was externally synced with the camera via a high-speed relay and acquired images at the same frame rate (up to 12,000 fps) with the Phantom camera.

Additionally, planar time-dependent radiation intensity measurement of the impinging jet was acquired using an infrared camera (FLIR SC6100) with an InSb detector. The view angle of the camera was aligned perpendicular to the flame axis (50 cm from the main chamber center to the camera lens) such that the half view angle of the camera was less than 10° . The radiation intensity detected by each pixel of the camera focal plane array was approximated by a parallel line-of-sight because of the small view angle. The spatial resolution was 0.2×0.2 mm² for each pixel. The bandpass filter was used to measure the radiation intensity of water vapor (2.58 ± 0.03 μm).

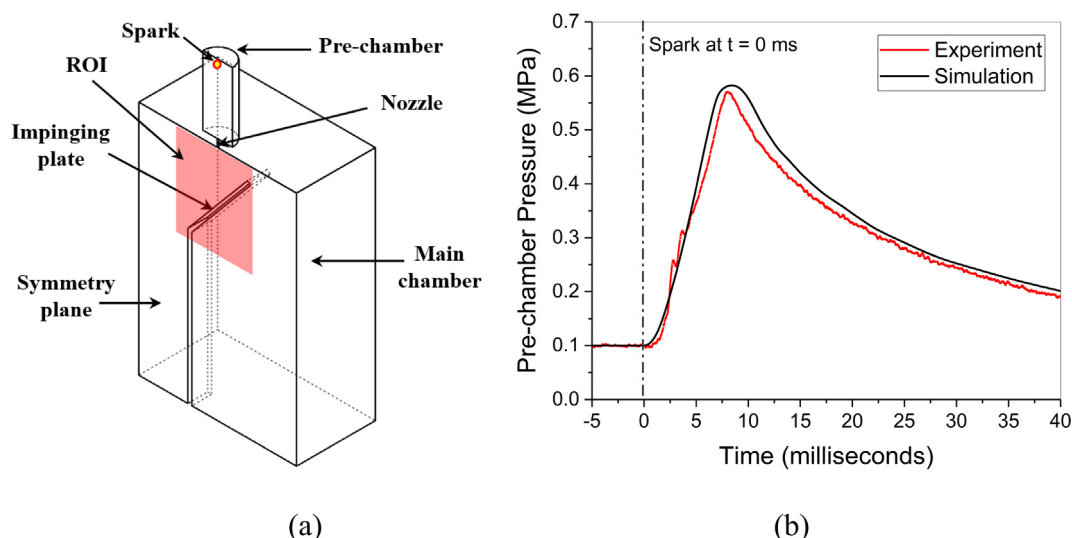


Fig. 2. (a) Schematic of the simulation domain for impinging jets, (b) pre-chamber pressure traces from the model and experiment.

3. Numerical modeling

The experimental results, which will be discussed shortly, showed that Plates 1, 4, and 6 initiated the main chamber combustion via the impinging jet ignition mechanism, while for the other plates the ignition mechanism was due to the classical jet ignition as has been discussed in our previous work [32]. To better understand at what conditions one ignition mechanism would dominate over the other, we numerically simulated the jet impingement process inside the non-reacting main-chamber. The purpose of the numerical simulations was not to compare the main chamber ignition behavior with the experiment, rather provide additional detailed information of the impinging jet, whose properties are critical towards understanding the ignition process without inferring additional complicacy due to main chamber combustion. Due to these reasons, we did not simulate the ignition and combustion processes in the main chamber. The main chamber reactions were switched off in the solver, whereas the reactions were active in the pre-chamber and the nozzle domain. The characteristics of the hot jet obtained numerically was studied at the time of the main chamber ignition measured experimentally.

The computational domain is shown in Fig. 2(a). Due to symmetry, only half of the 3D cylindrical pre-chamber, nozzle, and rectangular main chamber with the impinging plate were modeled. The pre-chamber and main chamber have the exact same dimensions as for the experiment [20]. The dimensions of the impinging plates are reported in Fig. 1(c). The entire domain except the boundary layer was discretized using Tetrahedron cells, whereas Hexahedron cells were used at the boundary. Five million cells were used in the computations. A mesh independence study was conducted on two different refined meshes – coarser and finer than the original mesh. A pressure outlet boundary condition was used at the nozzle outlet, while wall boundary conditions were applied elsewhere. The initial wall temperature was constant at 300 K with non-slip boundary condition. At the beginning of the simulation, a spark with an energy of 100 mJ was supplied at the specified spark location shown in Fig. 2(a) to initiate ignition in the pre-chamber.

Unsteady Reynolds Time-Averaged Navier-Stokes (U-RANS) equations coupled with mass, energy, and species conservation equations were solved using the commercial code ANSYS Fluent R15.0 [37]. The Reynold's Stress Models (RSM) coupled with detailed H_2 /air chemistry [38] (9 species and 21 elementary reactions) were implemented. The turbulence-chemistry interaction was modeled using the Eddy Dissipation Concept (EDC) model, which assumes that reaction occurs in small turbulent structures called the fine scales. This model has the

capability to include detailed chemical reaction mechanisms. The compressible Navier–Stokes equations were solved using a pressure-based solver in which the pressure and velocity were coupled using the Semi-Implicit Method for Pressure-Linked Equations (SIMPLE) algorithm. At the beginning of the simulation for a few milliseconds, a first-order upwind discretization scheme was used for the convective terms and turbulent quantities to obtain a stable, first-order solution. Once a stable solution was reached, we switched the discretization scheme to third order Monotone Upstream-Centered Schemes for Conservation Laws (MUSCL) for a more accurate solution. However, this higher order discretization scheme increased computation time significantly. The least squares cell-based gradient calculation scheme, which is known for accuracy and yet computationally less expensive, was chosen over the node-based gradient for the spatial discretization. A second order discretization scheme was used for pressure. The solution-adaptive mesh refinement feature was used to resolve flame front structure. A dynamic adaption of the temperature gradient was implemented to refine the mesh near the flame front or to coarsen it wherever needed. A fixed time step of $t = 10^{-6}$ second was used to resolve the chemical timescale, which was estimated to satisfy the Courant-Friedrichs-Lewy (CFL) condition for numerical stability. To attain a stable solution, we used a Courant number much less than unity. The second order implicit scheme was used for time integration of each conservation equation.

Fig. 2(b) compares the pre-chamber pressure histories from the simulation and experiment, which agreed well and provided validation for the numerical method. Both pressure histories show that after a short ignition delay of about 1.2 ms, the pre-chamber mixture was ignited, and the pressure started rising. The peak pressure, which is almost 6 times the initial pressure, occurred at about 9 ms after ignition. Afterward, pressure dropped as the pre-chamber combustion products entered the main chamber. The simulation reasonably agrees with the experiment, while the predicted pressure in the high-pressure region is slightly overestimated. This is likely caused by the leakage in the experiment which is not taken into account in the simulation.

4. Results and discussion

We first examined how the presence of various impinging plates affects the lean limit and ignition delay of the main-chamber mixture. Then, the main chamber ignition physics by an impinging jet were discussed based on simultaneous schlieren and OH^*OH^* imaging, along with infrared imaging which provided insights on the temperature distribution of the impinging jet. Additionally, the effect of nozzle diameter on the impinging jet ignition mechanism was discussed.

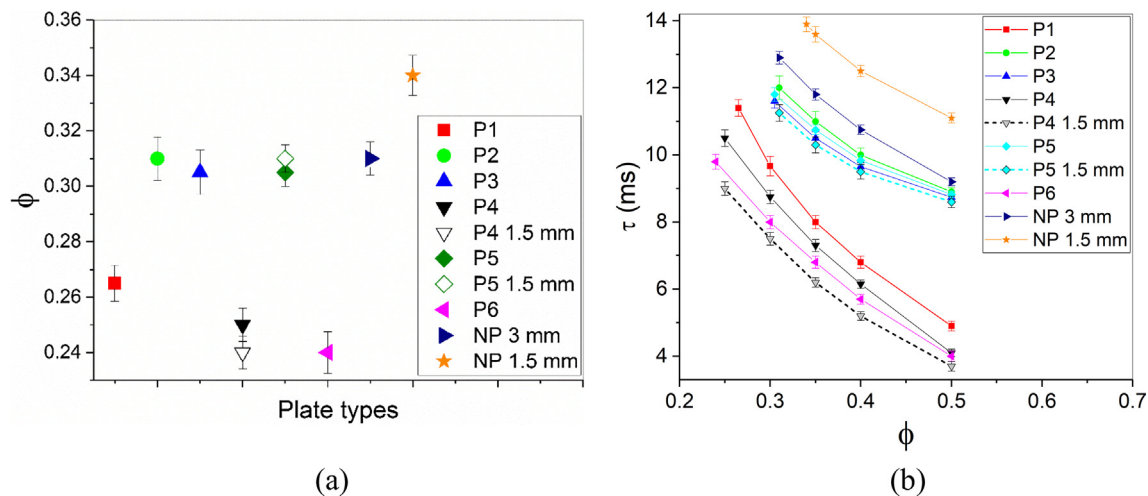


Fig. 3. (a) Flammability limit and (b) ignition delay of H_2 /air by impinging and turbulent jet ignition. ‘P’ and ‘NP’ denotes plate and no plate inside the main combustion chamber.

Lastly, numerical simulations of the impinging process were discussed, and an overall summary of the impinging jet dynamics was proposed.

4.1. Effect of impingement on main-chamber lean limit and ignition delay

As shown in our previous study [34] that without an impinging plate, the lean limit of the H_2 /air mixture in the main chamber that would result in the successful ignition was $\phi_{limit} = 0.31$. However, with an impinging plate, this limit can be reduced. For example, this limit was extended to $\phi_{limit} = 0.24$ for Plate 6 and $\phi_{limit} = 0.25$ for Plate 4. Fig. 3(a) plots the lean limit of different combinations of the impinging plate and nozzle diameter. To find the lean flammability limit, equivalence ratio was gradually decreased. For each equivalence ratio, 10 tests were carried out. As we go below the lean flammability limit, the mixture becomes unignitable. The error bar represents a zone within which ignition is possible. Out of the six impinging plates used, only Plates 1, 4 and 6 were able to extend the lean limit, while the presences of Plate 2, 3 and 5 did not change the lean limit as if there were no plates. Note Plates 1, 4 and 6 have the lowest H/D ratio, 18.5, 14.5, and 10 respectively, compared to the other plates. Additionally, two different nozzle diameters, 1.5 and 3 mm respectively, were used on Plates 4 and 5, and the results show that the 1.5 mm diameter nozzle can extend the lean limit for Plate 4 but not for Plate 5. As such, the nozzle diameter does not influence the ignition outcome (ignition by impingement or classical jet ignition), and a major factor is the H/D ratio. This will be elaborated further in later sections.

Fig. 3(b) shows the ignition delay for different plates. Ignition delay was defined as the time between the jet starts entering the main chamber and the onset of ignition in the main chamber. As expected, ignition delay decreased with increasing equivalence ratio for all cases. However, Plates 1, 4 and 6 produced shorter ignition delays in the main chamber for a given equivalence ratio than Plates 2, 3 and 5. The shorter ignition delay can be explained by the impinging jet ignition mechanism, that is, as soon as the hot jet hits the plate with sufficient momentum, the kinetic energy of the jet is reduced near the impinging location where the flow is nearly stagnant, increasing the local temperature. This creates an ideal environment for ignition to take place. This mechanism will be elaborated in detail in the later part of this paper.

Fig. 3(b) also plots the effect of nozzle diameters on ignition delay for Plates 4 and 5. The results from nozzle diameter 3 mm were compared to a nozzle diameter of 1.5 mm. When the ignition mechanism was due to jet ignition (Plate 5), the ignition delay remained the same. However, when the ignition occurred due to impingement, a smaller

nozzle produced a lower ignition delay. To understand this behavior, we examined the impingement physics of the jet which will be discussed in following sections.

4.2. Two ignition mechanisms

Fig. 4 shows the time sequence of the ignition process in the main chamber for different impinging plates using high-speed schlieren (top) and OH^* chemiluminescence (bottom). It is clear for Plates 1, 4 and 6 the ignition started from the surface of the impinging plate, i.e., around the stagnation point where the hot jet hits the plate. This indicates that as the hot turbulent jet impinged onto the plate, the kinetic energy was transferred into thermal energy. Thus, the temperature around the stagnation point increased, which led to the ignition of ultra-lean mixture in the main chamber. However, for Plates 2, 3, 5 the ignition occurred at the upstream of the impinging point. The ignition mechanism is the same as what we previously found [20], that is, ignition happens on the lateral sides of the jet before it hits the impinging surface. In this case, the mixing process between the jet consisted of hot combustion products and the cold unburned ambient mixture fundamentally determines the ignition outcome. Clearly, for the two sets of plates, the ignition mechanism is quite different. We will call the first mechanism “impinging jet ignition mechanism” to separate it from the conventional “jet ignition mechanism.” We found for a nozzle diameter of 3 mm the maximum impinging distance was 2.2 in. that could result in ignition by the impinging jet ignition mechanism, above which the conventional jet ignition mechanism dominated. Moreover, this distance changed for different nozzle diameter. But as we scaled the impinging distance, H by the nozzle diameter, D , we found that there exists a limiting H/D ratio below which impinging jet ignition occurs. Additionally, for Plate 6, $H1.2 \approx 90^\circ$, as the jet split into two by the vertical Plate 6, the jet started to slow down due to boundary effect, and ignition started from the boundary layer on the Plate 6.

Comparing the two ignition mechanisms, we found that the impinging jet ignition mechanism resulted in much lower ignition delay than the conventional jet ignition mechanism. As shown in Fig. 4, for identical experimental conditions, the former mechanism (Plates 1, 4 and 6) has ignition delay ranging from 4 to 4.8 ms compared to the latter (Plates 2, 3 and 5) ranging from 8.7 to 8.9 ms. In other words, the ignition delay was significantly lowered when the ignition was initiated due to impingement.

Fig. 5 shows the time history of the heat release rate (HRR) for different plates at the lean limit. Fig. 3(b) already discussed the ignition delay resulting from different plate configurations. The HRR

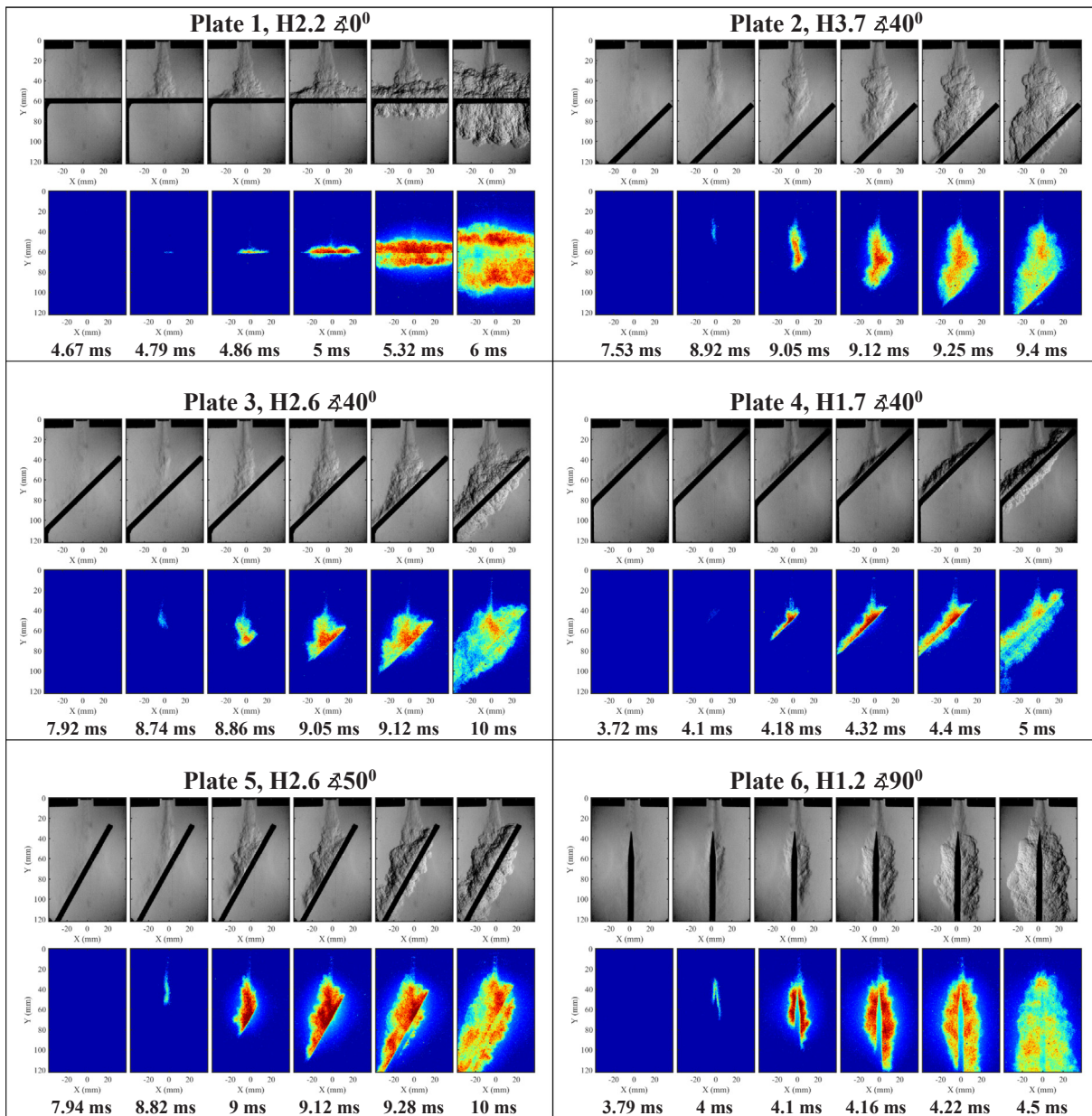


Fig. 4. The time sequence of simultaneous schlieren (top) and OH* chemiluminescence (bottom) images showing ignition process of H₂/air for different impinging plates. Experimental conditions for all test cases: $V_{pre-chamber} = 100$ cc, $D_{nozzle} = 3$ mm, $P_{initial} = 0.1$ MPa, $T_{initial} = 300$ K, $\phi_{pre-chamber} = 1.0$, $\phi_{main chamber} = 0.4$.

calculations were based on the experimental pressure trace and Swaminathan’s HRR correlation [39] for premixed combustion. It is interesting to notice that plate 1, 4, and 6 have higher heat release rate than the others. Moreover, the heat release is much faster for these plates compared to the others. This could indicate that the initial flame kernel development is faster due to impinging jets, as compared to typical turbulent jet ignition. Thus, for plates 1, 4, and 6, where ignition was initiated by jet impingement, the heat release became faster, and the rate was higher.

Fig. 6 shows simultaneous planar time-dependent radiation intensity measurements and high-speed schlieren imaging of the jet impingement process. It is evident that Plates 1, 4 and 6 show an elevated intensity near the impingement region, whereas, for the other plates, radiation intensity decreases monotonically in the streamwise direction along the jet axis. Moreover, the length of this high-intensity region increases with the impinging angle. For example, the high-intensity region is much smaller for Plate 1 (0° impinging angle) compared to Plate 4 (40° impinging angle). The radiation intensity measurement of

the impinging region, as shown in Fig. 7(b), explains why Plates 1, 4 and 6 could ignite via impinging jet ignition mechanism, whereas the other plates failed to do so. Fig. 7(a) illustrates the local ζ - η coordinate, where the ζ axis is along the plate, and the η axis is normal to the plate. The radiation intensity near the stagnation region at $\eta = 2$ mm is plotted in Fig. 7(b) for the six plates just before ignition in the main chamber. It is clear that the radiation intensity for Plates 1, 4 and 6 is much higher than that for the other plates, indicating higher temperature in that region. In other words, an elevated temperature region was created near the impinging region for Plates 1, 4, and 6. Moreover, as shown in Fig. 7(b), the length of this elevated temperature region is shorter for impinging angle 0° compared to 40° and 90°. For Plate 6 (90° impinging angle), the radiation intensity is maximum at the plate tip and quickly decreases with increasing ζ . While the radiation intensity profile shows symmetry for Plates 1 and 6, Plate 4 has an asymmetric radiation intensity profile, due to the angled impingement. This behavior can also be seen from the numerical simulation results addressed in the next section.

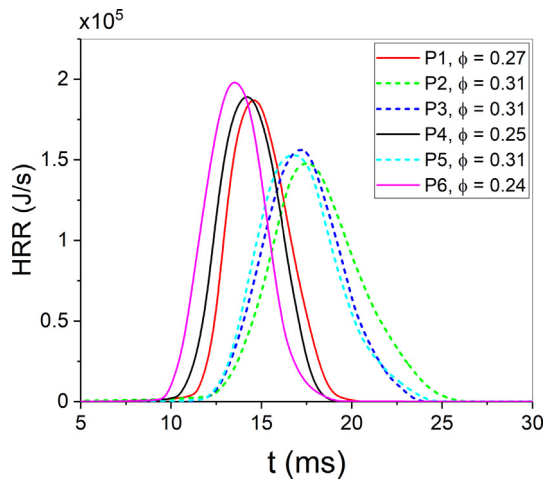


Fig. 5. Time history of average heat release rate (HRR) for different plates at their respective lean flammability limit.

4.3. Numerical simulation results

Fig. 8 plots the velocity, pressure, temperature, and fuel mass fraction distributions of the flow for the six plates. Note the results shown correspond to the moment just prior to ignition occurred in the main chamber. The purpose was to compare the velocity, pressure, temperature, and fuel mass fraction distributions to understand why Plate 1, 4 and 6 were able to lower the lean limit of the main-chamber mixture for successful ignition. The fuel mass fraction, χ was defined as,

$$\chi = \frac{Y_{H_2}}{Y_{H_2}|_{Ub}} \tag{1}$$

where Y_{H_2} is the mass fraction of H_2 in the mixture and $Y_{H_2}|_{Ub}$ is the initial mass fraction of the unburned H_2 at $t = 0$ in the main chamber.

Fig. 8 shows that the static pressure increases at the stagnation point for Plates 1, 4 and 6. Moreover, the stagnation point moves upward on the plate with an increase in the plate angle and distance from the nozzle exit. For these plates, main chamber ignition was always initiated from the region between ‘OS’ as shown in Fig. 8 (streamlines on

static pressure contour). Additionally, a temperature increase was observed near the stagnation region for Plate 1, 4 and 6, which was absent for other plates. The fuel mass fraction indicates the mixing process between the hot jet and the cold ambient. Looking at the fuel mass fraction, χ , for Plates 1, 4 and 6, the mixing started to occur near the impinging region. For other plates, the jet was well-mixed with the cold ambient before it impinged on the plate. Since main chamber reactions were switch off in the solver, a well-mixed jet and ambient suggests an ignition occurred further upstream of the impinging surface. Thus, for Plates 2, 3, and 5, ignition occurred by classical turbulent jet ignition mechanism.

Fig. 9 plots the numerically calculated static pressure, static temperature, turbulent dissipation, velocity, and vorticity magnitude at three distinct locations, $\eta = 0.04, 0.5$ and 1.0 mm from the impinging surface for the six impinging plates. For Plates 1, 4 and 6 the static pressure and temperature increases significantly near the stagnation region compared to other three plates. Around the similar region, the turbulent dissipation and the vorticity magnitude increases as well. Thus, for Plates 1, 4 and 6 the turbulent jet has a higher local temperature, vorticity, and turbulent dissipation. Therefore, for these plates, a superior mixing zone was created near the stagnation region. This led to ignition in the region near the stagnation point and also explains why Plates 1, 4 and 6 resulted in lower lean limit of the main chamber mixture. Lastly, for identical impinging angle, a larger ‘OS,’ which is the distance between the geometric center and the stagnation point, signifies that the static pressure and temperature will be distributed over a larger area. Thus, the initiation of ignition could start from a distributed region near the impinging surface and thus enhanced the ignition probability. This was the reason why Plate 4 could achieve a lower lean limit for both nozzle diameters, 1.5 mm and 3 mm, than all the other plates.

4.4. Impinging jet dynamics

The experimental and numerical results both suggest that if the impinging plate is placed closer to the nozzle exit, ignition will likely be initiated near the impinging point where the flow is nearly stagnant, and the local temperature and mixing are increased, all of which provide an ideal environment for ignition to take place. If the impinging plate is placed far away from the nozzle exit, then the plate will have

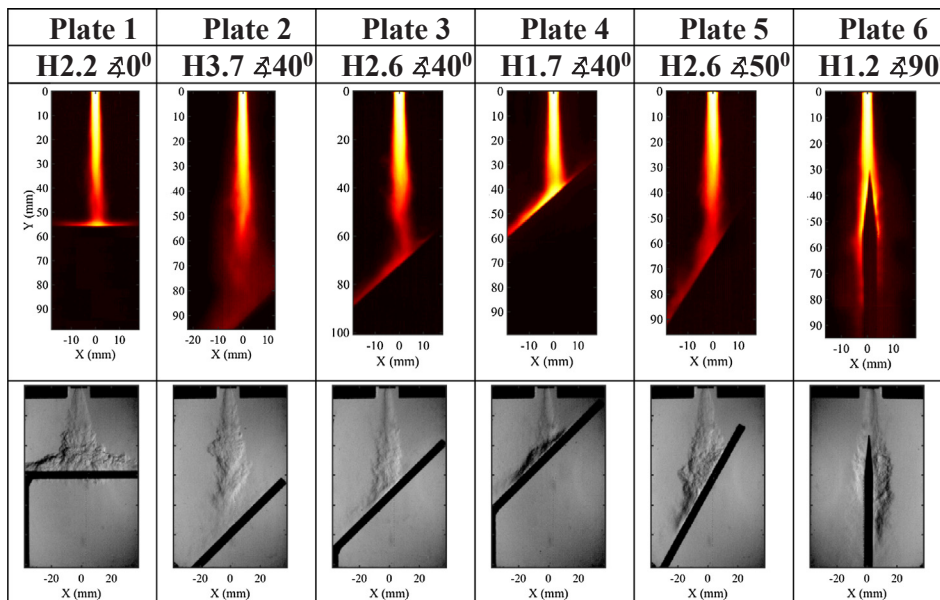


Fig. 6. Infrared (top) and schlieren images (bottom) showing the hot turbulent jet impinging on the surface just before ignition in the main chamber. Test conditions: $V_{pre-chamber} = 100$ cc, $D_{nozzle} = 3$ mm, $P_{initial} = 0.1$ MPa, $T_{initial} = 300$ K, $\phi_{pre-chamber} = 1.0$, $\phi_{main chamber} = 0.4$.

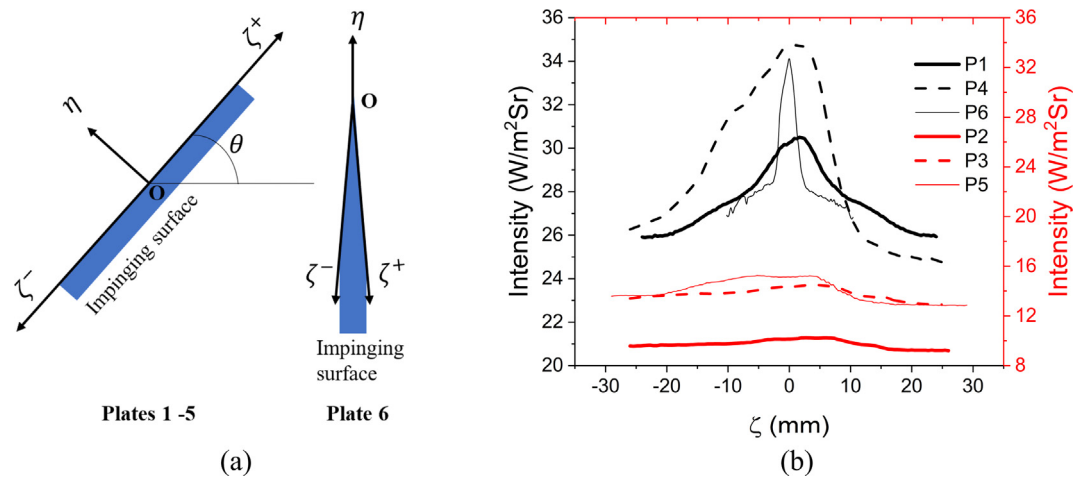


Fig. 7. (a) The local η - ζ coordinate. (b) Radiation intensity at $\eta = 2$ mm for different impinging plates from nozzle diameter of 3 mm.

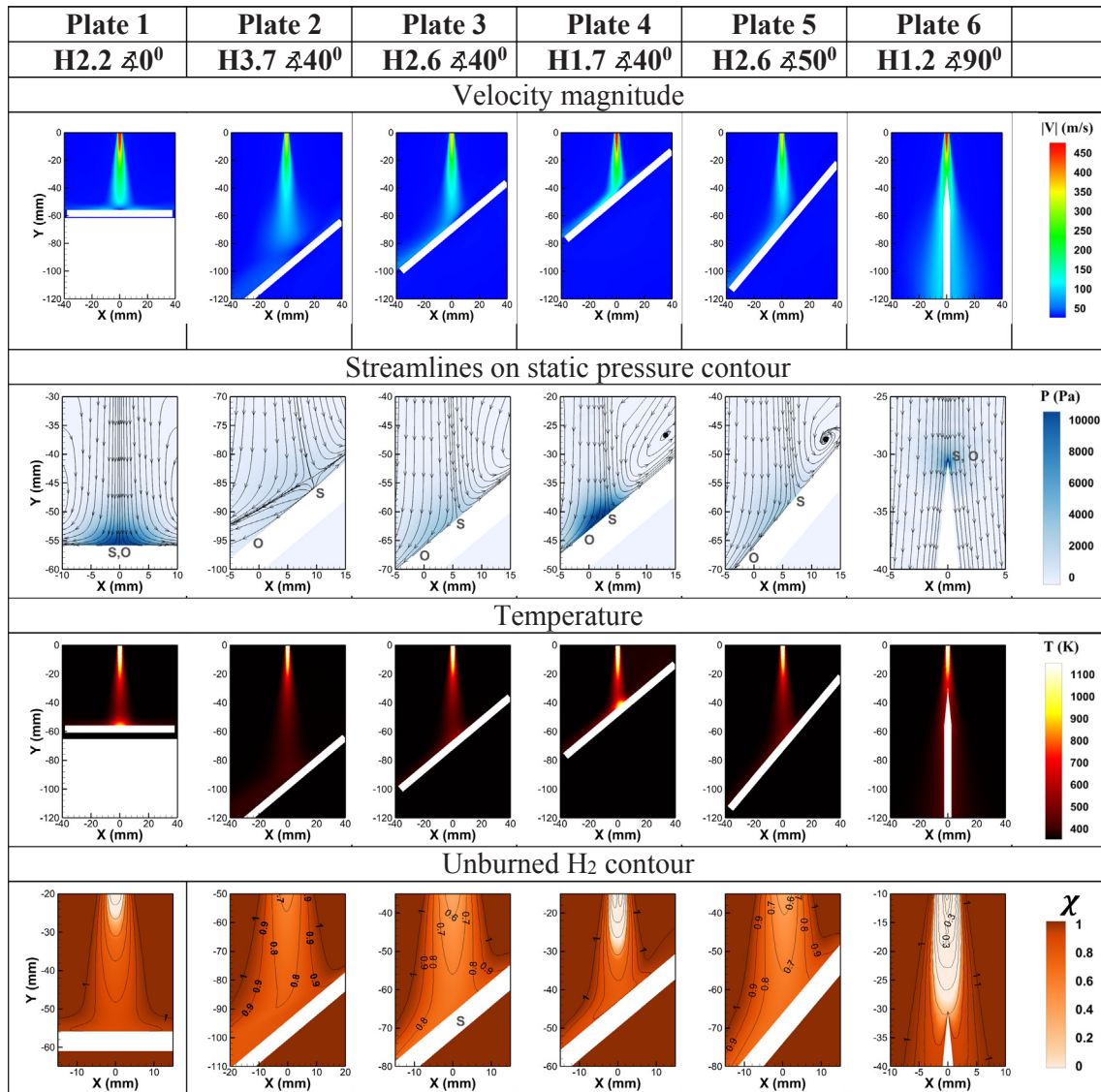


Fig. 8. Numerically simulated velocity field, streamlines on static pressure field contour, temperature field, and fuel mass fraction ratio, χ just before ignition in the main chamber for H₂/air for impinging plates 1 – 6. Test conditions: $V_{pre-chamber} = 100$ cc, $D_{nozzle} = 3$ mm, $P_{initial} = 0.1$ MPa, $T_{initial} = 300$ K, $\phi_{pre-chamber} = 1.0$, $\phi_{main chamber} = 0.4$.

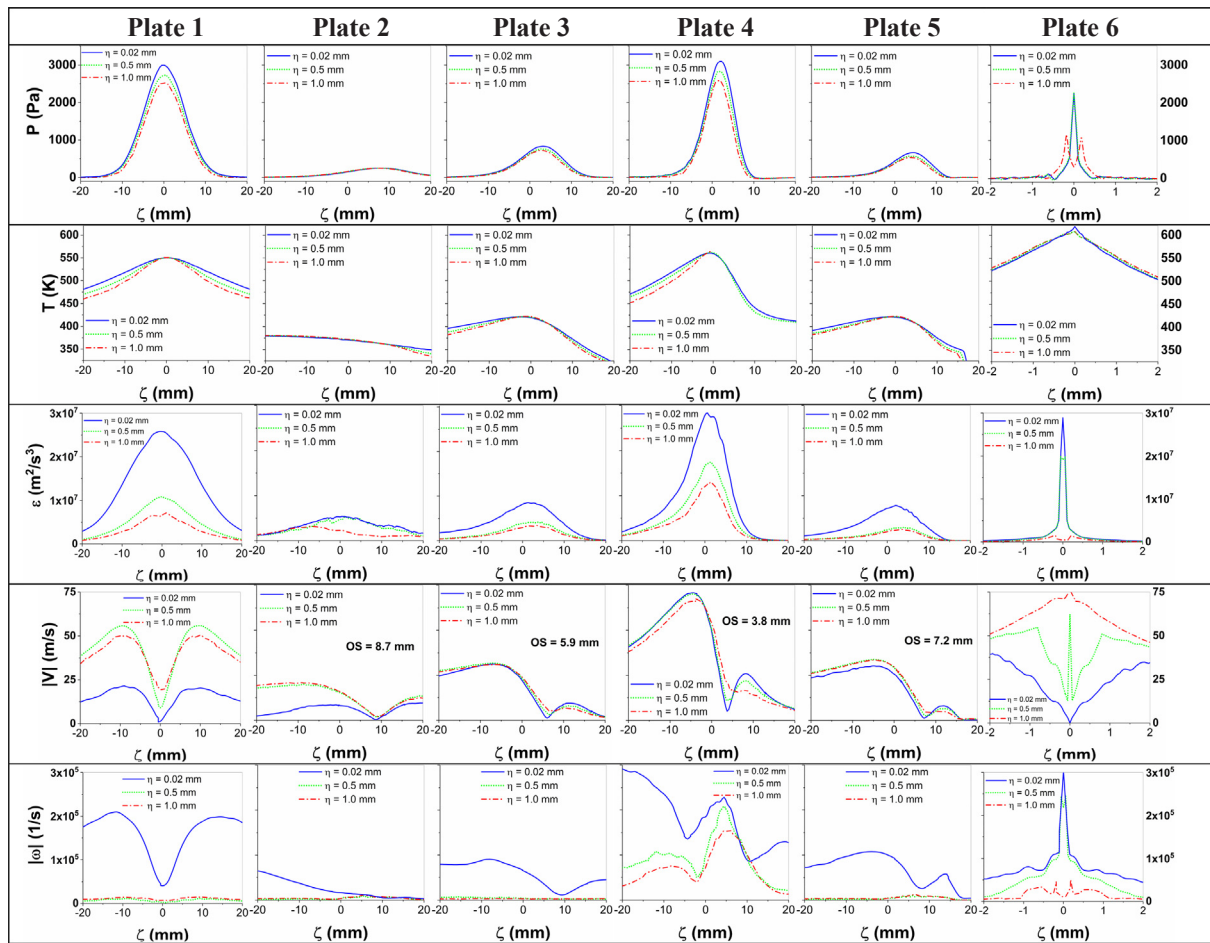


Fig. 9. Numerically calculated static pressure, static temperature, turbulent dissipation, velocity, and vorticity magnitude at three distinct locations, $\eta = 0.04, 0.5$ and 1.0 mm from the impinging surface corresponding to Fig. 8 test conditions.

minimum influence on the ignition of the main-chamber mixture which is determined by the mixing process between the hot jet and the cold ambient. To better understand how impinging jets could potentially extend the lean limit, we examined the fluid dynamics, heat and mass transfer in and around the impinging region.

Fig. 10(a) shows the schematic of a jet impinging on an inclined surface. For a plate placed normal to the impinging direction such as Plate 1, the stagnation point ‘S’ coincides with ‘O,’ the geometric center of the impinging plate. As the impinging angle increases, the stagnation point starts to move upward [28]. Fig. 10(b) supports this observation, which shows a hot turbulent jet of Reynolds number 27,450 impinged on a plate with an inclination angle of 40° and the stagnation point shifted upward on the plate. The shifting can be noticed from the higher intensity of the IR image occurred at the upstream of the geometric center ‘O’ and well as from numerical results. OH^* image shows the location from where the ignition initiated in the main chamber. Our numerical results show that the static pressure increase is maximum between ‘O’ and ‘S.’ Interestingly, ignition in the main chamber started from the region between ‘O’ and ‘S.’

As shown in Fig. 10(a), when the hot turbulent jet impinges on the plate, the jet comes to a standstill at the stagnation point. The jet velocity in the stagnation region slows down considerably. Due to a sudden change in the flow direction, the vorticity in the impinging region increases. After a while, the turbulent jet becomes reattached to the plate in the wall jet region. However, between the stagnation and wall jet region, the jet narrows down and the mixing increases. For a turbulent jet with Reynolds number higher than 15,000, local mixing pockets arise in this narrow wall jet region [28]. Through this region,

the unburned fuel/air can mix well with the turbulent jet. All the kinetic energy in the high velocity hot turbulent jet converts into thermal energy at the stagnation point. Thus, the dynamic temperature rise occurs at the stagnation point ‘S.’ Due to enhanced mixing the unburned fuel/air entrains in the hot jet through impinging region. If the unburned fuel/air arrives near to this stagnation region, due to high-temperature condition at the stagnation region, ignition occurs. Lastly, it was observed that ignition by an impinging jet always started from the zone, ‘OS,’ and the ignition mechanism depends on two key parameters, H/D ratio, and the impinging angle, θ .

The effect of H/D ratio and impinging angle, θ is shown in Fig. 11. To examine the effect of H/D ratio, a variety of nozzle diameters ranging from 0.75 to 4.5 mm (0.75, 1, 1.5, 2, 2.25, 3, 4.5 mm) were used in combination with six different impinging plates. The ignition mechanism corresponding to all this H/D combinations is plotted on Fig. 11(a). Using Fig. 11(a) we could find a limiting H/D ratio that separates two different ignition mechanisms – classical turbulent jet ignition and impinging jet ignition. The range of H/D ratio for which impinging jet ignition occurs is $4 < H/D < 21.6$. For a H/D ratio, $21.6 < H/D < 74.8$ ignition occurs via turbulent jet ignition mechanism. Thus, the critical H/D ratio required for impinging jet ignition to occur is $H/D_{critical} \leq 21.6$. Fig. 11(b) shows the effect of the impinging angle, θ . The effect of three different impinging angles, $\theta = 0^\circ, 40^\circ$ and 90° were explored for a constant H/D ratio of 14. The impinging angle did not affect the ignition mechanism; however, the impinging angle affected the main chamber burn time, time to consume the entire fuel/air mixture in the main chamber. We found that the highest impinging angle, $\theta = 90^\circ$ produced the smallest burn times and the smallest

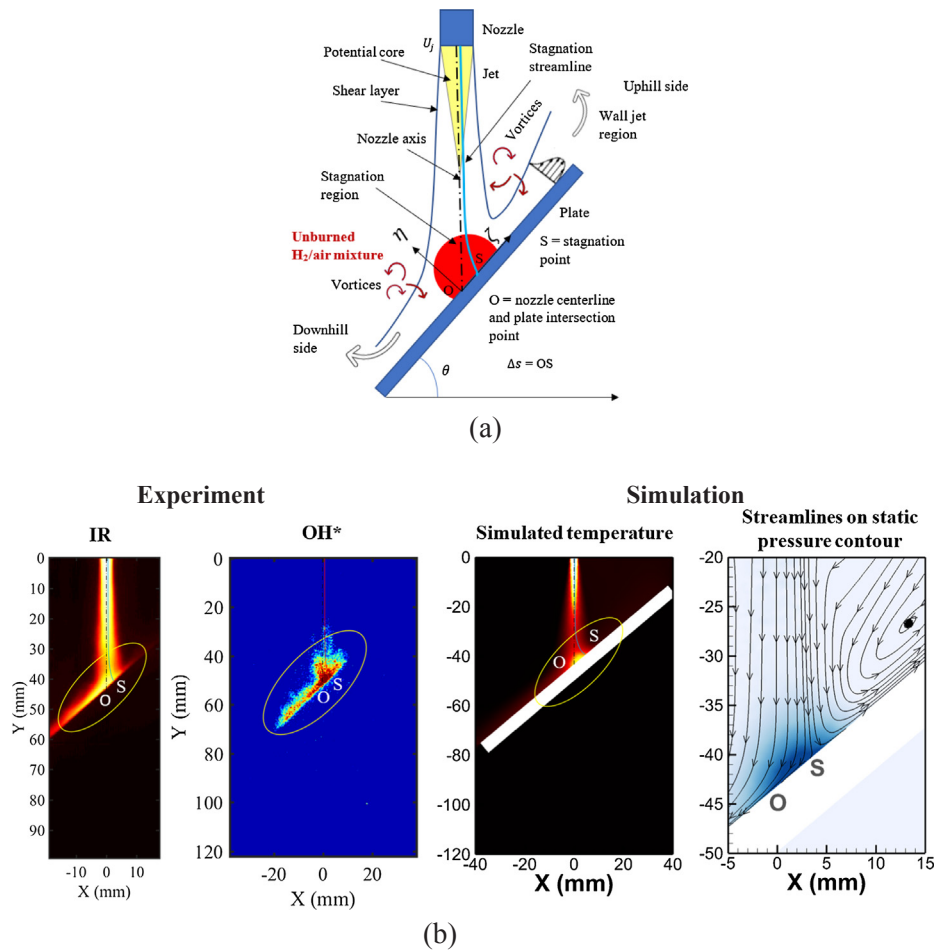


Fig. 10. (a) Impinging jet dynamics, (b) velocity, temperature and static pressure field around the stagnation point.

impinging angle, $\theta = 0^\circ$ resulted in the longest burn times. Thus, the burn time increases with decreasing impinging angle. The effect of impinging angle can be understood looking at the distance ‘OS’ as shown in Fig. 10(a). We found ignition by impingement always initiates from ‘OS,’ i.e. the distance between the stagnation point and the geometric center of the impinging surface. This distance ‘OS’ increases with an increasing impinging angle. The distribution of static pressure and

temperature increase near the stagnation region occurs over the ‘OS.’ Thus, with an increasing impinging angle ignition initiates from a longer region ‘OS.’ Since the length of the initial ignition kernel is longer on an impinging plate with larger inclination angle, this helps the main chamber flame to quickly propagate and consume the main chamber fuel/air and hence resulted a shorter burn time.

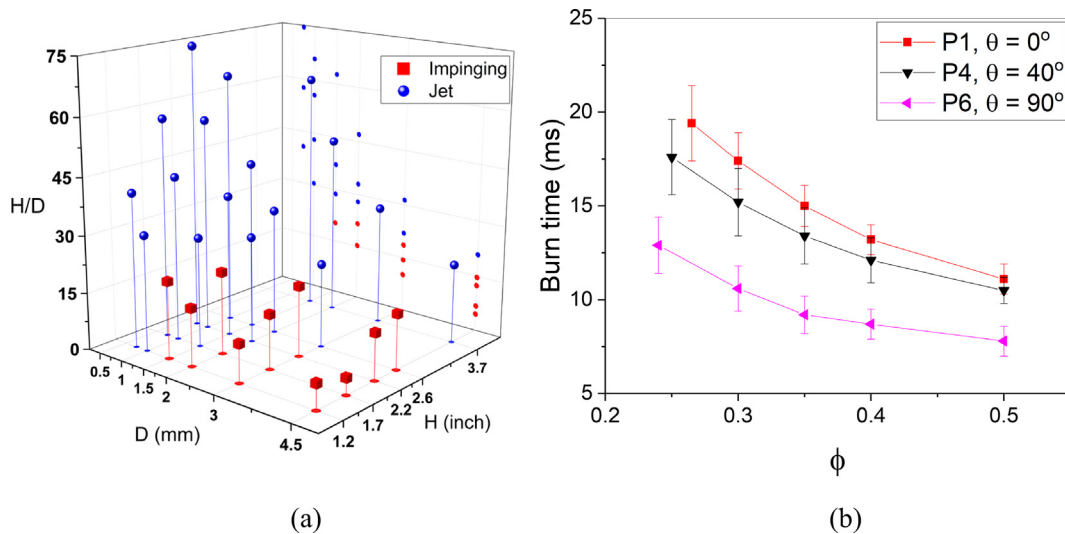


Fig. 11. The effect of (a) H/D ratio, and (b) impinging angle.

5. Conclusions

The present study investigated the ignition characteristics of ultra-lean H_2 /air mixtures using an impinging hot turbulent jet generated by pre-chamber combustion experimentally and numerically. The major findings are summarized below.

1. Impinging jet ignition can extend the lean limit of H_2 /air mixture in the main chamber, as compared to conventional turbulent jet ignition. This is because the impinging jet creates a high-pressure, high-temperature stagnation zone near the impinging region which provides an ideal environment for ignition. Moreover, increasing vorticity near the impinging region allows better mixing between the unburned, fresh fuel/air in the main chamber and the hot burned gases in the stagnation region. The higher temperature and enhanced mixing, combined, are the reason why impinging jet can extend the lean limit of the main chamber mixture. Furthermore, impinging jet ignition reduces the ignition delay in the main chamber compared to classical turbulent jet ignition.
2. Two key parameters related to impinging jet ignition are the ratio of impinging distance to the nozzle diameter, H/D ratio and the impinging angle, θ . The impinging angle does not affect the ignition mechanism. The ignition mechanism is solely controlled by the H/D ratio. The limiting H/D ratio for impinging jet ignition to occur is $H/D_{critical} \leq 21.6$ that separates impinging jet ignition from classical turbulent ignition.
3. The impinging angle, however, affects the main chamber burn time. The burn time decreases with increasing the impinging angle. As the impinging angle is increased, the distance between the geometric center and the stagnation point 'OS' increases. Thus, the thermal energy spreads over a larger 'OS,' which facilitates initiation of distributed ignition. Thus, the main chamber burn rate increases with increasing impinging angle.

References

- [1] Murase E, et al. Initiation of combustion in lean mixtures by flame jets. *Combust Sci Technol* 1996;113(1):167–77.
- [2] Karimi A, Rajagopal M, Nalim R. Traversing hot-jet ignition in a constant-volume combustor. *J Eng Gas Turbines Power* 2013;136(4):041506.
- [3] Lee M, et al. Planar fluorescence imaging of a transverse jet in a supersonic cross-flow. *J Propul Power* 1992;8(4):729–35.
- [4] Reddy H, Abraham J. Ignition kernel development studies relevant to lean-burn natural-gas engines. *Fuel* 2010;89(11):3262–71.
- [5] Gussak LA. The role of chemical activity and turbulence intensity in Prechamber-Torch organization of combustion of a stationary flow of a fuel-air mixture. In: International congress & exposition, Detroit, Michigan; 1983.
- [6] Oppenheim AK. Quest for controlled combustion engines. In: International congress and exposition, Detroit, Michigan; 1988.
- [7] Wolfhard HG. The ignition of combustible mixtures by hot gases. *J Jet Propul* 1958;28(12):798–804.
- [8] Ghoniem AF, Oppenheim AK, Chen DY. Experimental and theoretical study of combustion jet ignition. California University; 1983.
- [9] Pitt PL, Ridley JD, Clemilnts RM. An ignition system for ultra lean mixtures. *Combust Sci Technol* 2007;35(5–6):277–85.
- [10] Yamaguchi S, Ohiwa N, Hasegawa T. Ignition and burning process in a divided chamber bomb. *Combust Flame* 1985;59(2):177–87.
- [11] Sadanandan R, et al. Detailed investigation of ignition by hot gas jets. *Proc Combust Inst* 2007;31(1):719–26.
- [12] Toulson E, Watson H, Attard W. Gas assisted jet ignition of ultra-lean LPG in a spark ignition engine. SAE technical paper 2009-01-0506; 2009.
- [13] Gholamisheeri M, Wichman IS, Toulson E. A study of the turbulent jet flow field in a methane fueled turbulent jet ignition (TJI) system. *Combust Flame* 2017;183:194–206.
- [14] Attard W et al. Spark ignition and pre-chamber turbulent jet ignition combustion visualization. SAE technical paper 2012-01-0823; 2012.
- [15] Gentz G, Gholamisheeri M, Toulson E. A study of a turbulent jet ignition system fueled with iso-octane: pressure trace analysis and combustion visualization. *Appl Energy* 2017;189:385–94.
- [16] Perera I, Wijeyakulasuriya S, Nalim R. Hot combustion torch jet ignition delay time for ethylene-air mixtures; 2011.
- [17] Carpio J, et al. Critical radius for hot-jet ignition of hydrogen–air mixtures. *Int J Hydrogen Energy* 2013;38(7):3105–9.
- [18] Shah A, Tunestal P, Johansson B. Effect of pre-chamber volume and nozzle diameter on pre-chamber ignition in heavy duty natural gas engines; 2015. p. 1.
- [19] Vedula RT, et al. Thermal efficiency of a dual-mode turbulent jet ignition engine under lean and near-stoichiometric operation. *Int J Engine Res* 2017;18(10):1055–66.
- [20] Biswas S, et al. On ignition mechanisms of premixed CH_4 /air and H_2 /air using a hot turbulent jet generated by pre-chamber combustion. *Appl Therm Eng* 2016;106:925–37.
- [21] Ghorbani A, et al. Ignition by transient hot turbulent jets: an investigation of ignition mechanisms by means of a PDF/REDIM method. *Proc Combust Inst* 2015;35(2):2191–8.
- [22] Gussak LA, Turkish M, Siegl D. High chemical activity of incomplete combustion products and a method of prechamber torch ignition for avalanche activation of combustion in internal combustion engines. SAE technical paper 750890; 1975.
- [23] Chitsaz I, et al. Experimental and numerical investigation on the jet characteristics of spark ignition direct injection gaseous injector. *Appl Energy* 2013;105:8–16.
- [24] Attard WP et al. A new combustion system achieving high drive cycle fuel economy improvements in a modern vehicle powertrain. SAE technical paper 2011-01-0664; 2011.
- [25] Nerheim LM. Prechamber for a gas engine. Rolls-Royce Marine: US 20100132660 A1; 2011.
- [26] Herold H et al. Pre-combustion chamber tip. Caterpillar Motoren GmbH & Co. Kg: US 8813716 B2; 2014.
- [27] Viskanta R. Heat transfer to impinging isothermal gas and flame jets. *Exp Therm Fluid Sci* 1993;6(2):111–34.
- [28] Martin H. Heat and mass transfer between impinging gas jets and solid surfaces. *Adv Heat Transf* 1977;13:1–60.
- [29] Tajik AR, Hindasageri V. A numerical investigation on heat transfer and emissions characteristics of impinging radial jet reattachment combustion (RJRC) flame. *Appl Therm Eng* 2015;89:534–44.
- [30] Wang Q, Zhao CY, Zhang Y. Time-resolved 3D investigation of the ignition process of a methane diffusion impinging flame. *Exp Therm Fluid Sci* 2015;62:78–84.
- [31] Biswas S, Qiao L. Prechamber hot jet ignition of ultra-lean H_2 /air mixtures: effect of supersonic jets and combustion instability. *SAE Int J Eng* 2016;9(3).
- [32] Biswas S, Qiao L. A numerical investigation of ignition of ultra-lean premixed H_2 /air mixtures by pre-chamber supersonic hot jet. *SAE Int J Eng* 2017;10(5):2231–47.
- [33] Biswas S, Qiao L. A comprehensive statistical investigation of schlieren image velocimetry (SIV) using high-velocity helium jet. *Exp Fluids* 2017;58(3):1–20.
- [34] Biswas S, Qiao L. Ignition of ultra-lean premixed H_2 /air using multiple hot turbulent jets generated by pre-chamber combustion. *Appl Therm Eng* 2018;132(5):102–14.
- [35] Biswas S. Physics of turbulent jet ignition: mechanisms and dynamics of ultra-lean combustion. 1st ed. Springer; 2018.
- [36] Biswas S, Qiao L. Combustion Instabilities of Ultra-Lean Premixed H_2 /Air Mixtures by Pre-chamber Turbulent Jet Ignition. *J Propul Power* 2018.
- [37] ANSYS. ANSYS Fluent Academic Research, Release 15.0; 2015.
- [38] Kéromnès A, et al. An experimental and detailed chemical kinetic modelling study of hydrogen and syngas mixtures at elevated pressures. *Combust Flame* 2013;160(6):995–1011.
- [39] Swaminathan N, et al. Heat release rate correlation and combustion noise in premixed flames. *J Fluid Mech* 2011;681:80–115.